Title
Morphing the Body Shape of an Underwater Walking Robot to Improve Hydrodynamic Loading

Permalink
https://escholarship.org/uc/item/5251593m

Author
Ishida, Michael

Publication Date
2018

UNIVERSITY OF CALIFORNIA SAN DIEGO

Morphing the Body Shape of an Underwater Walking Robot to Improve Hydrodynamic Loading

A Thesis submitted in partial satisfaction of the
requirements for the degree
Master of Science

in

Engineering Sciences (Mechanical Engineering)

by

Michael Ishida

Committee in charge:

Professor Michael T. Tolley, Chair
Professor Nicholas Gravish
Professor Andrew J. Lucas

2018

The Thesis of Michael Ishida is approved, and it is acceptable in quality and form for publication on microfilm and electronically:

Chair

University of California San Diego

2018

DEDICATION

To family, friends, and the knowledge that there’s always next season.

EPIGRAPH

What is now proved was once only imagined.

—William Blake, *The Marriage of Heaven and Hell*

TABLE OF CONTENTS

LIST OF FIGURES

LIST OF TABLES

ACKNOWLEDGEMENTS

I would like to acknowledge my committee chair and PI Prof. Michael T. Tolley for providing guidance throughout the entire project and MS degree process.

I would also like to acknowledge the members of the Bioinspired Robotics and Design Lab for advice and feedback on the project and for making lab life enjoyable.

This thesis, in part, is currently being prepared for submission for publication of the material. Ishida, Michael; Drotman, Dylan; Shih, Benjamin; Hermes, Mark; Luhar, Mitul; Tolley, Michael T. The thesis author was the primary investigator and author of this material.

ABSTRACT OF THE THESIS

Morphing the Body Shape of an Underwater Walking Robot to Improve Hydrodynamic Loading

by

Michael Ishida

Master of Science in Engineering Sciences (Mechanical Engineering)

University of California San Diego, 2018

Professor Michael T. Tolley, Chair

Many platforms have been developed for moving remotely underwater; however, many of these systems are limited to traversing open water and must expend large amounts of energy to maintain a position in flow for long periods of time. Legged animals are common in nature, but often have fixed body morphologies restricting them to constant hydrodynamic profiles. This work presents an underwater legged robot with soft legs and a soft morphing body for manipulating the hydrodynamic forces in flow. Computational fluid dynamics (CFD) simulations of the morphing body in flow allow 1) prediction of the effect of morphing on lift and drag forces, and thus 2) determination of which body configuration is most favorable for specific tasks. Flow over the morphing body separates behind the trailing edge which determines where turbulence begins to form, causing additional drag. When the legged robot needs to remain stationary in flow, a flat structure offers reduced hydrodynamic forces for resisting sliding. When the legged robot needs to walk with flow, a larger inflated body is pushed along by the flow, causing that robot to walk faster than it would otherwise. A commercial force sensor can detect flow so that the robot can respond by morphing into a more advantageous shape. Experiments with the prototype robot are used to test these capabilities.

Chapter 1

Introduction

Underwater locomotion techniques employed by man-made and biological systems differ significantly. Manned submersibles and remotely operated vehicles (ROVs) often use either jet propulsion [1] or rotating propellers [2] to move through the water. These strategies work well in open water, but systems that use these mechanisms are bulky and noisy compared to many biological counterparts and cannot navigate through confined spaces. A few biological organisms also use jet propulsion [3], but many more move by undulating their bodies or oscillating their fins [4]. Although useful mechanisms for swimming, these techniques require expending large amounts of energy on propulsion to remain stationary in flow when examining a surface or taking long duration measurements. In contrast, many marine organisms that live on underwater surfaces like reefs or in tidepools employ a form of legged locomotion using rigid appendages [5] or hydraulic tube feet [6] that overcome the aforementioned limitations.

The morphology and locomotion behaviors of animals suggest the importance of hydrodynamic characteristics in underwater walking. Legged stability on land is determined primarily by the distribution of weight over the legs, but stability in water is also affected by fluid forces like buoyancy, lift, and drag [7]. This difference has a large impact on legged locomotion in these two domains. Amphibious newts, for example, alter their gaits when transitioning from land to water so that their legs spend less time planted on the surface generating large amounts of drag in the more dense fluid [8, 9]. Crabs have rigid exoskeletons that have less drag along one axis than the other and have evolved gaits that take advantage of that preferentially biased shape. Those with less drag along the horizontal axis walk sideways, while those with less drag along the forward axis walk forward [10]. Crabs searching for a food odor source orient themselves toward the odor source when walking in low flow, but orient themselves in the hydrodynamically preferable direction when walking in high flow, even to the detriment of odor detection [11]. Furthermore, sea stars displaced by researchers from a low-tidal area to a high-tidal area showed a change in arm aspect ratio that lowered drag coefficient and thus pull-off force [12].

Morphing structures are flexible elements that can actively change shape during system operation. Many marine organisms use morphing structures to dynamically change their interactions with flow [13]. Small fish have fins that deform as they swim [14] while octopuses and squid create large body deformations to both propel and maneuver their bodies [15]. Similar morphing structures have been used in robotics such as in the octopus-inspired PoseiDRONE [16] and in robots designed by artificial evolution [17]. Soft skins can change the 2D appearance and texture of a surface into preprogrammed 3D Gaussian structures [18]. The compression and decompression of different cells on the skin of a robot to morph the surface and alter the direction bias of a central actuator was used to create a soft mobile robot for hole or pipe traversal [19]. Morphing elements were used in the flippers of a turtle-inspired swimming robot to produce both twisting and flapping motions similar to those of a real turtle [20]. Similar morphing elements in the wings of a bat-inspired flying robot allowed the system to increase lift during the wings' downstrokes and to decrease drag during the wings' upstrokes [21].

Controlling a shape-changing structure requires the knowledge of the effect of different shapes on hydrodynamic forces. Computational fluid dynamics (CFD) simulations have been used to determine the effects of structures on underwater vehicles [22] and robotic crab shells [23] as well as on robot legs [24] or swimming paddles [25]. In addition, CFD simulation has

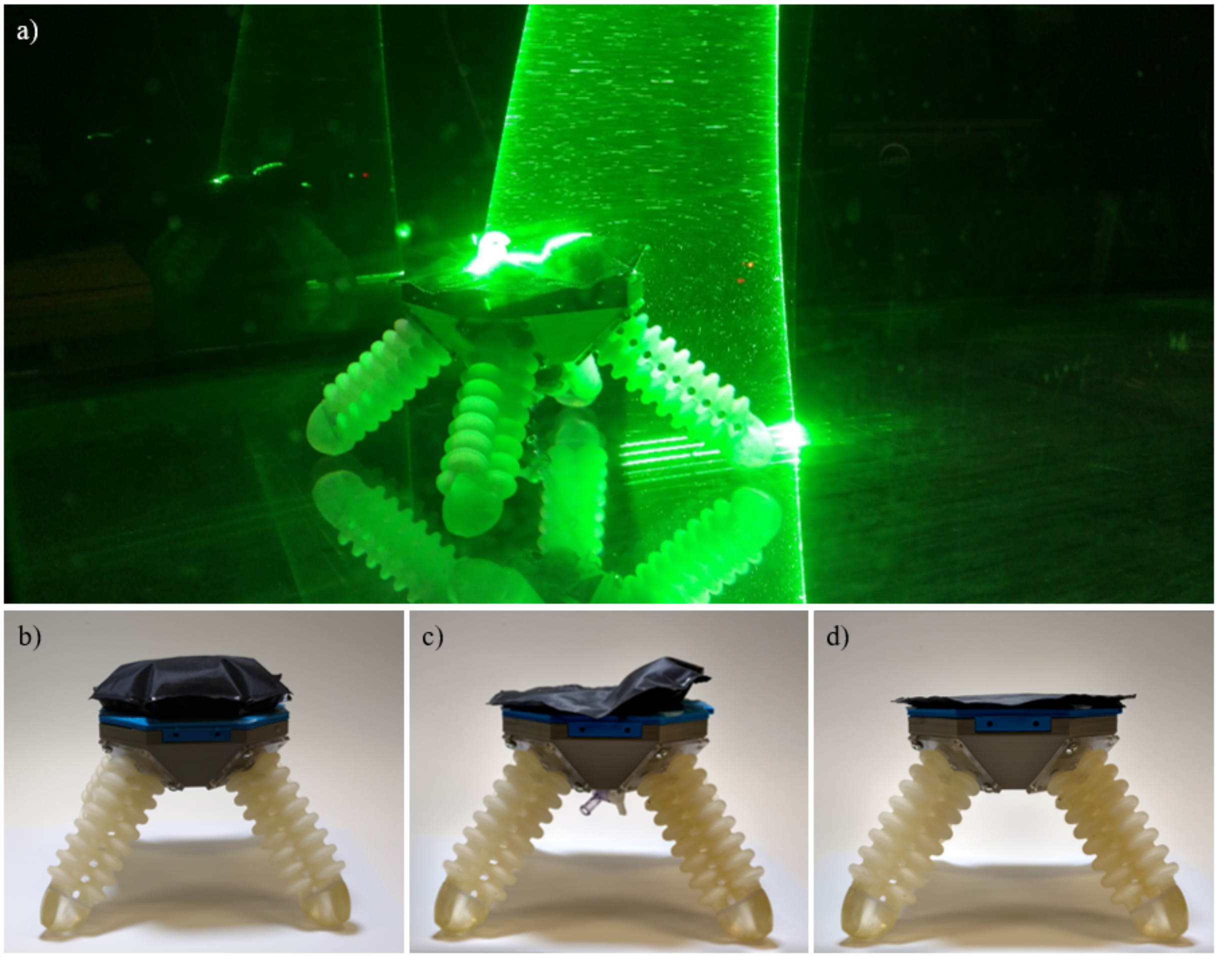

Figure 1.1: Soft quadruped robot for walking underwater with morphing structure that changes shape to be more hydrodynamically advantageous based on force sensor readings. a) Robot with morphed structure in flow illuminated by particle image velocimetry laser. b) Robot with symmetric morphing body. c) Robot with asymmetric morphing body. d) Robot with flat body.

also been used to determine the effect of control inputs on the forces experienced by actuators [26] and the effect of posture change on propulsion elements [27].

Soft robotics is a growing subfield of intelligent systems that leverages inherent material compliance to create highly adaptable robots [28]. These systems often use fluidic elastomer actuators (FEAs), which are enclosed chambers made of hyperelastic materials that change shape when supplied with positive or negative fluid pressure. Flexible but inextensible materials constrain the actuators and dictate their movements when subjected to an internal pressure change, while maintaining system compliance [29, 30, 31, 32]. The material flexibility and compliance of soft actuators give them infinite degrees-of-freedom and create movement on a continuum scale [33]. Robots using these components can adapt to their environments much more readily than rigid robots can, which allows them to perform actions like conforming to irregular surfaces and objects [34]. This behavior is especially beneficial for a legged walking system, as a soft actuator can bend to variety of different configurations that would require many joints to replicate in a rigid system [35]. In addition, continuum actuation creates smooth surfaces instead of blunt edges or sharp corners that are advantageous for interactions with fluids [36].

Previous work on underwater walking robots has primarily focused on using traditional robotics techniques to create rigid jointed walkers. The six-legged AQUAROBOT was developed for measuring seabottom roughness via pressure sensors in the feet of the robot [37]. An inexpensive autonomous legged underwater vehicle was created for locating mines with touch sensors as a largely independent agent in a swarm [38]. Little Crabster, another six-legged robot with rigid mechanisms was developed specifically for exploring shallow water in high tidal environments [39]. To test an underwater walking gait based on the punting gait of a crab, a one-legged robot was designed and showed a self-stabilizing locomotion mode combining swimming and pushing gaits [40], while a different bioinspired crab robot was created to analyze the underwater dynamics and fluid forces on the swimming, walking, and punting gait of a hybrid robot [41]. However, none of the aforementioned underwater walking robots leverage soft robotics, which would allow these designs to better traverse uneven terrain and could create additional novel gaits that are impossible with rigid appendages.

The hydrodynamics of a structure in contact with flow is an important design consideration for dynamic underwater systems, so I introduce here a soft robot capable of sensing local flow conditions and morphing a portion of its body to maintain a hydrodynamically advantageous profile (Figure 1.1). The shape of the body is altered using soft fluidic actuators that switch the body profile between different states with different hydrodynamic characteristics. A commercial off-the-shelf force sensor is used to determine the direction of the flow, allowing the robot to opportunistically change its body shape. When walking in the same direction as the flow, the robot can increase the force of drag on its body and when walking in still water or against flow it can decrease the force of drag. In addition, under higher velocity flow the robot can increase the downward lift force, or downforce, on the body to give it additional traction.

In Chapter 2, I describe the design of the soft hydraulic quadruped robot and the mechanisms that control its actuation while in Chapter 3, I detail the experimental methods used to test the robot. In Chapter 4, I discuss the effect of different robot bodies attached to the same legged base on robot traction in flow and in Chapter 5, I discuss the effect of the robot shape in dynamic environments. Finally, in Chapter 6 I present some conclusions and future work.

Chapter 2

Soft Robot Design

The Bioinspired Robotics and Design Lab has previously presented a soft quadrupedal robot capable of navigating unstructured terrain in air [42]. That robot used positive air pressure to actuate its legs in a predetermined sequence, with different pressurization sequences and timing causing different gaits that can be tailored to the type of terrain. In the present work, I have made a new version of this robot that uses hydraulics and associated hardware instead of pneumatics for walking underwater.

2.1 Actuators for Locomotion

The soft fluidic actuators used for the robot legs are printed using a commercially available multimaterial 3D printer (Connex3, Stratasys) out of a photocured rubber (TangoPlus) [42]. Each flexible actuator consists of three parallel bellowed chambers arranged in a radially symmetric pattern; these chambers extend when positive pressure is applied and contract when negative pressure is applied. The bellowed geometry allows the actuators to compress and extend axially through a folding and unfolding process, which compensates for the fact that the 3D printed material (Shore hardness 70A) has a lower yield strain than most other elastomers commonly used in soft robotics.

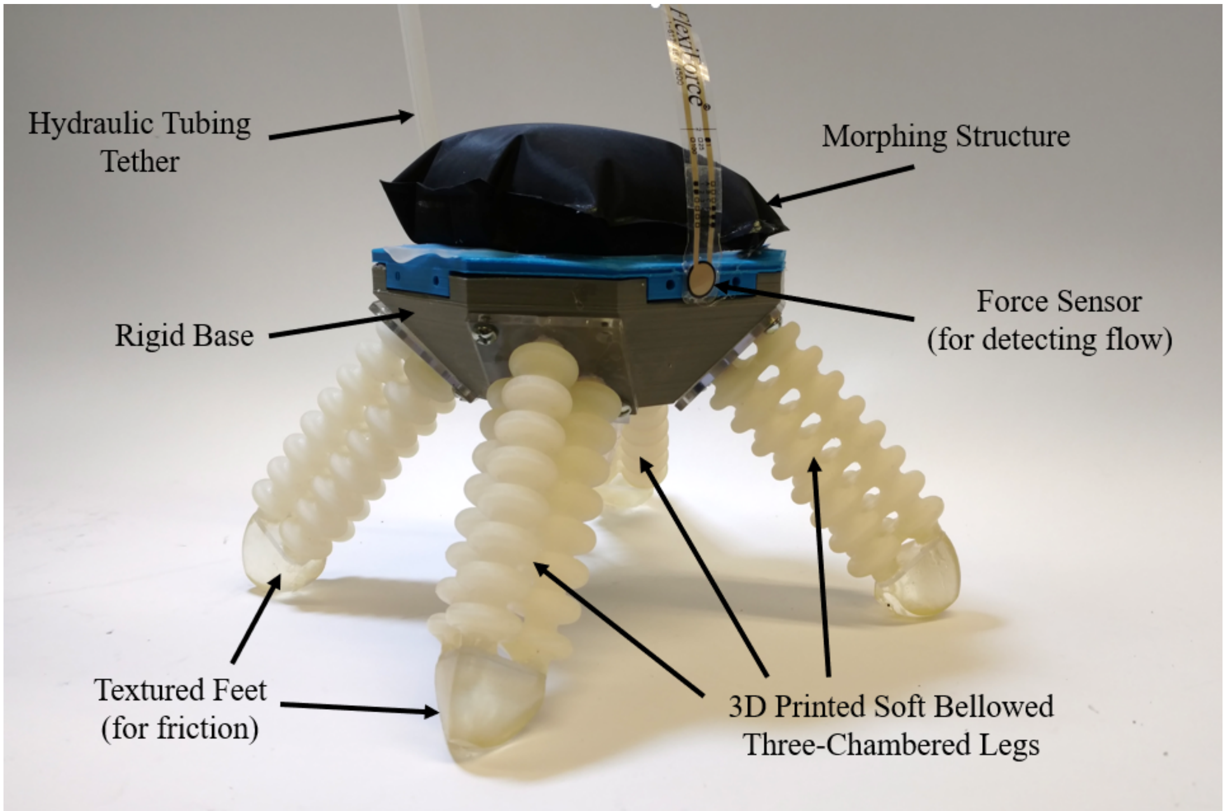

Figure 2.1: Annotated image of the soft quadruped with morphing structure.

When a chamber is pressurized, the bellowed material unfolds and the chamber extends. However, the three chambers are connected along the centerline which constrains the extension of each chamber so pressurization causes a net bending motion. If a single chamber is pressurized, the actuator bends away from that chamber and if two chambers are pressurized, the actuator bends toward the third chamber. When pressure in the chamber is released, the actuator relaxes back toward its neutral position. By systematically and cyclically inflating the chambers of the four legs, the legs bend in a repeatable pattern, creating a walking gait. Changing the order of chamber pressurization and the duration of pressurization and relaxation will change the gait.

Attached to the end of each leg actuator is a rounded and textured tip made of the same material as the legs that acts as a foot. This piece increases the friction between the leg and the ground, limiting sliding during actuation, particularly on smooth surfaces. High friction between the robot and the ground resists lateral forces on the robot caused by flow and increases traction. In addition, the increased traction gives the robot additional grip on the surface from which to push off during the walking gait.

2.2 System Electronics

The Bioinspired Robotics and Design Lab designed the system presented in [42] for use on land using pneumatic pressure for leg actuation. For operation underwater, I used hydraulic hardware instead of pneumatic hardware to prevent the buoyancy effects caused by using air as a working fluid. An off-the-shelf pump and solenoid valve system supplies hydraulic pressure to the robot and were chosen to meet pressure, flowrate, and availability needs. Since operation of the legs requires a consistent connection to a pressure source, a tether of flexible tubing connects the robot to the land-based hydraulic hardware. Four three-way solenoid valves switched between pressurizing and venting chambers of each leg and two other valves switched between pressurizing and venting of the morphing structure. The legs were actuated cyclically, with each pair of legs diagonally opposite each other actuated as a couplet. Within each diagonal couplet, the first stroke causes the top chambers push the legs downward, followed by a lateral stroke that pulls the robot forward. Changing the length of time that each chamber is pressurized changes the amount that each leg bends, while changing the length of time between strokes changes how much elastic energy in the leg material is dissipated. An Arduino Mega microcontroller and a set of MOSFETs produce the time-synchronized signals that control the solenoid valves in the pattern needed to achieve the desired gait.

The pneumatic gait switched directly between inflation of the first couplet to inflation of the other couplet, which assumes that the first couplet can depressurize to the neutral position in the time it takes to inflate the second couplet. This is not the case when using water as a working fluid since water is much more dense than air is and adds a significant time constant to the system. The pressurization stroke of the gait stroke has the hydraulic pump acting as a high pressure driver, whereas the depressurization stroke relies on the differential between the internal actuator pressure and the ambient pressure to drive flow. This causes the depressurization stroke to be much slower than the pressurization stroke, necessitating delays between the actuation of each couplet to provide additional time for the actuator to return to the neutral position.

A commercial off-the-shelf force sensor is adhered to the front of the robot to detect flow. The sensor consists of two metal disks and conductive traces; when flow applies a force to the sensor, the disks move closer together and the resistance between them decreases. Sensing changes in the flow allows the robot to respond by morphing its structure. However, this requires calibration between the force sensor readings and the speed of the flow encountered. This sensor detected changes in flow above and below a given threshold rather than measuring absolute values of the flow rates encountered.

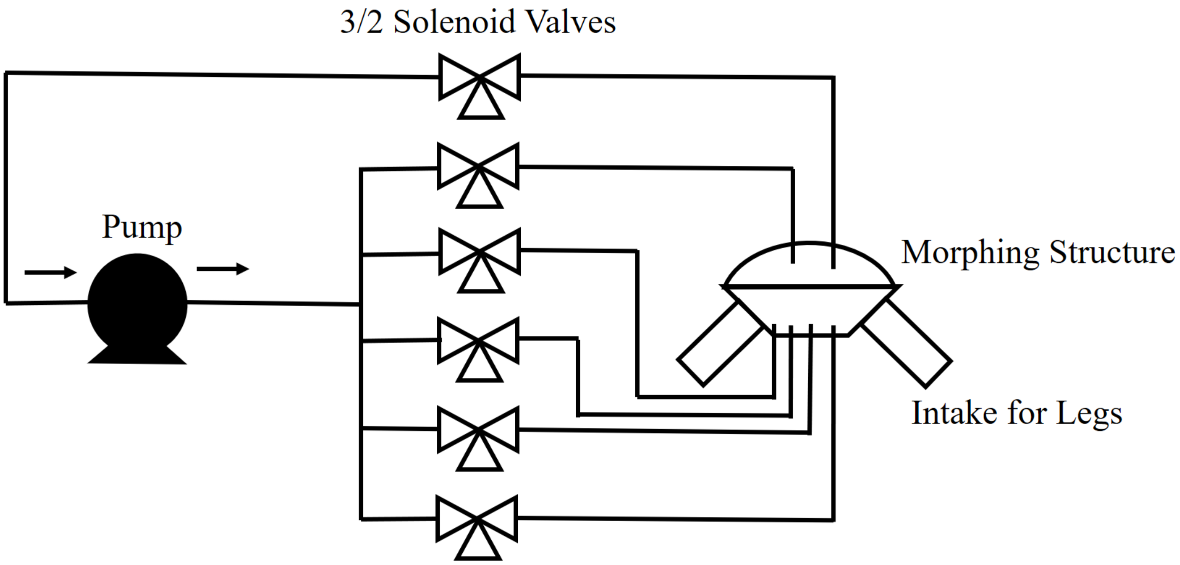

Figure 2.2: Diagram of the hydraulic setup. Four three-way solenoid valves control the inflation and venting of the legs and two other valves control inflation and vacuuming of the morphing structure.

2.3 Body and Morphing Structure

A rigid, 3D printed (Replicator 5, MakerBot) frame holds the four legs at a 45° angle relative to the ground. This forms the lower part of the body and is made of an inflexible material to ensure a consistent angle between the leg and the frame. Previous iterations of the robot had a wireframe structure, but for use underwater I replaced the wireframe structure with a solid frame to eliminate turbulence caused flow hitting internal geometries of the wireframe. The new frame also includes a hole in one of the back faces to allow the hydraulic tubing tether to exit the body.

An inflatable pouch forms a soft morphing structure on top of the 3D printed frame that changes the hydrodynamic characteristics of the robot as needed. To fabricate the pouch, I attached two sheets of taffeta fabric together using an impulse sealer to trigger heat-activated adhesives along the edges of the pouch, forming an enclosed volume. I then inserted a fitting and a tube into one of the sheets of fabric, through which a positive or negative pressure source can enlarge or contract the pouch. To finish, I adhered the edges of the pouch to a rigid cover that I bolted to the rigid frame. By adjusting the size, shape, and spatial orientation of the pouch, I can create different morphed surfaces on the robot body.

I created three body shapes to explore different hydrodynamic profiles. When uninflated, the morphing structure forms a flat surface on the top of the robot. When the robot pressurizes the smaller of the two pouches, the pouch forms an inflated structure covering half of the robot body; when the robot pressurizes the larger pouch, the inflated structure covers the entire surface. Since the robot cannot inflate the two pouches at the same time, the overall height of the fully and semi-morphed structures are constant (Fig. 2.3). I chose these basic shapes because they were simple to fabricate and representative of different potential profiles for the robot body.

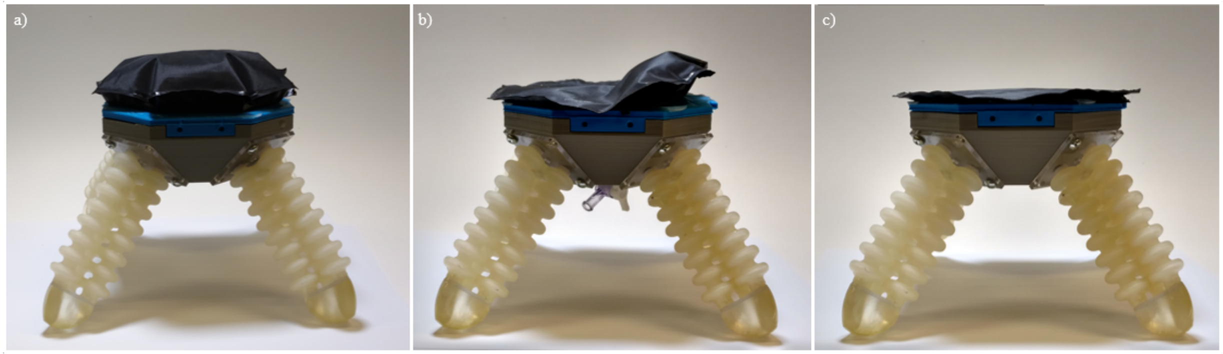

Figure 2.3: Diagram of the actuator, reprinted from the introduction. a) The large-morph body shape where the morphing structure is inflated across the entire width of the body. b) The semi-morph body shape where the morphing structure is inflated across half the width of the body. c) The flat body shape where the morphing structure is uninflated.

The fluid forces of drag and lift on the body are functions of the body shape, the density of the fluid, the cross-sectional area of the body in contact with the flow, and the fluid velocity around it. By inflating and deflating the morphing structure on top of the body, the robot changes its shape and its cross-sectional area, changing both drag and lift. A shape change that increases the downward lift on the robot will likely also increase the drag, indicating that it is difficult to decouple the two factors. When walking in the same direction as flow, increasing drag will increase the walking speed of the robot; when walking against flow, increasing drag will decrease its walking speed. Increasing the downward lift will increase the ground reaction force applied to the legs, which in turn increases the friction between the ground and the feet of the robot. Increasing the upward lift will decrease the ground reaction force applied to the legs, lessening the friction between the ground and robot, causing it to more easily slide or move upward.

To predict the critical velocity U_C at which the underwater walking robot begins to slip, consider a simple force balance. Assuming that the drag force $F_d = \frac{1}{2} C_D \rho A U_C^2$ generated by the fluid and the static friction $F_f = \mu N$ at the leg-substrate interface are in balance at the point of incipient motion the following represents the force balance of the system:

$$\frac{1}{2} C_D \rho A U_C^2 = \mu N = \mu \left[(M - \rho V) g - \frac{1}{2} \rho C_L A U_C^2 \right] \tag{2.1}$$

where C_D and C_L are the drag and lift coefficients for the morphing body (respectively), A, V, and M are the frontal area, volume, and mass of the robot (respectively), μ is the static friction coefficient for the leg-substrate contact, ρ is the density of the surrounding fluid, and g is the acceleration due to gravity. Rearranging the expression above yields the following expression for the critical velocity:

$$\frac{1}{2} \rho \left(C_D + \mu C_L \right) A U_C^2 = \mu (m - \rho V) g \tag{2.2}$$

$$U_C = \sqrt{\frac{2\mu (M - \rho V) g}{\rho A (C_D + \mu C_L)}} \tag{2.3}$$

Thus, to increase the critical velocity, a soft robot capable of morphing could change the frictional contact to increase μ, decrease frontal area A, or alter the shape to decrease $C_D + \mu C_L$. So in addition to minimizing the drag coefficient C_D by morphing into a smooth hydrodynamically-efficient shape, another viable strategy is to alter its shape to generate downforce ($C_L < 0$) rather than lift.

Chapter 3

Experimental Methods

3.1 Water Channel

With collaborators, I conducted the experiments measuring the critical velocity for sliding and the particle image velocimetry (PIV) measurements in the freshwater channel in the Fluid-Structure Interactions Lab at the University of Southern California (see Fig. 3.1). The channel is 762 cm long and 91 cm wide with a water depth of 48 cm. The maximum flow velocity of the channel is $60\,\mathrm{cm/s}$ with a background turbulence level of less than 1% and is changed by adjusting an analog dial. The ambient fluid temperature in the channel is 23 °C, which corresponds to a kinematic viscosity of $0.93 \times 10^{-2}\,\mathrm{cm^2/s}$. Flow conditions differ a maximum of 5% along the width of the channel. Additional testing of the robot walking and of flow measurement with the force sensor was done in the Environmental Fluid Dynamics Lab at the University of California, San Diego.

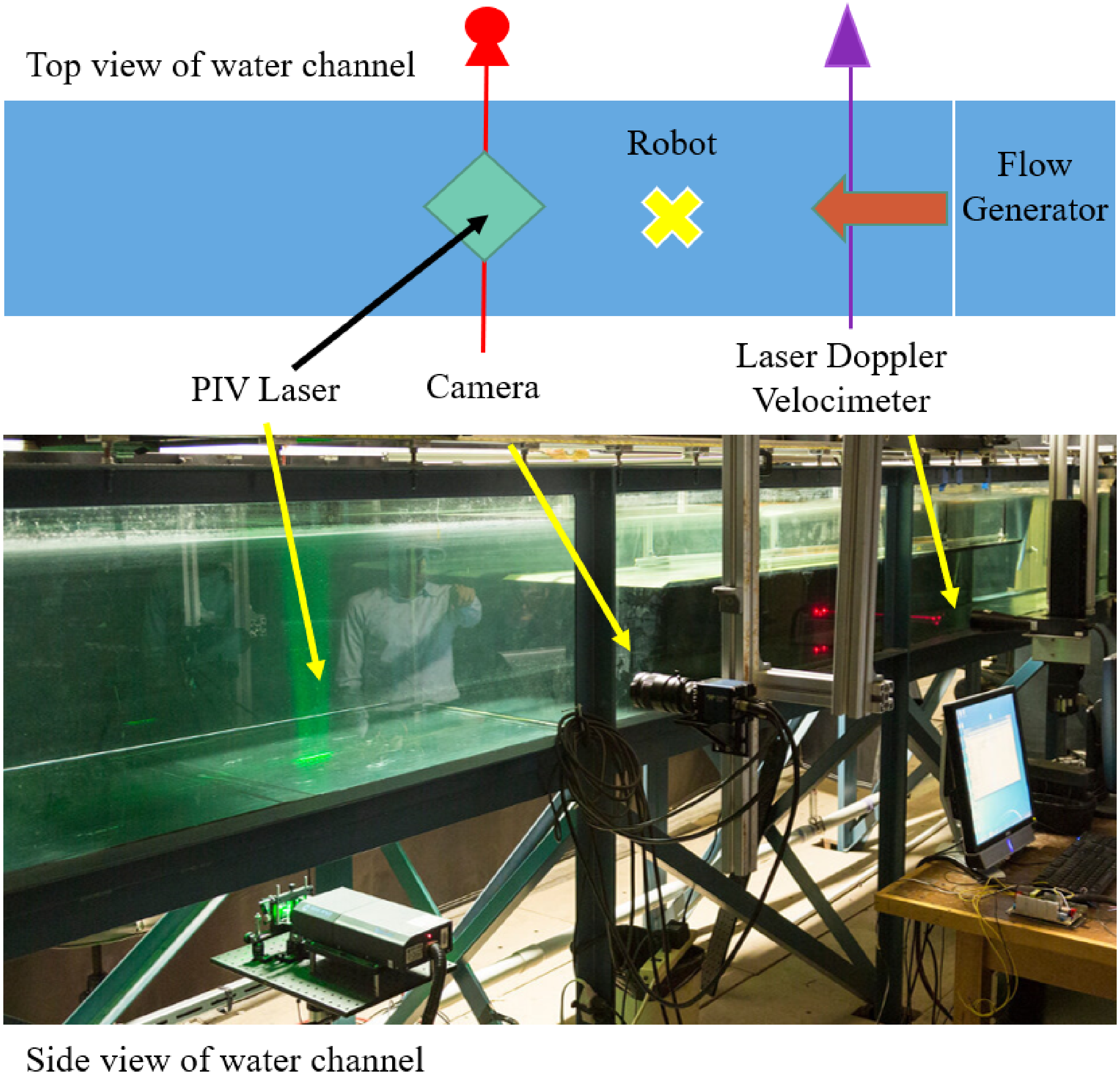

Figure 3.1: Top view diagram and side view image of the water channel in the Fluid-Structure Interactions Lab at the University of Southern California with labeled instrumentation. The labeled instrumentation remained outside the channel, not submerged in the water.

3.2 Instrumentation

We measured flow velocity using laser Doppler velocimetry (LDV) in the region of the channel near the robot and at the bottom of the channel to better estimate the reduced flow speed in the boundary layer along the channel floor where the robot would be walking. Stationary cameras positioned perpendicular to the channel pointing at the robot from both the side and the bottom followed the robot as it walked through the channel. The side-view camera recorded the position of the robot in the horizontal direction of desired movement and in the vertical direction to examine lift or downforce generated by flow over the morphed structure while the bottom-view camera recorded the out-of-plane movement to give an accurate measurement of the total velocity through the channel.Iused open-source optical tracking software (Tracker, Open Source Physics) to determine the position and speed of the robot from videos taken by the stationary cameras by tracking a given point on the robot body. After identifying a characteristic feature of the robot and measuring the length of that feature, the software could then calibrate distances in the video with actual lengths.

In addition, we measured and imaged the fluid velocity field around the robot using a particle image velocimetry (PIV) system. A green laser projected a light sheet into the water, scattering off silver particles in the channel. A high-speed black-and-white camera mounted to the side of the channel captured images of the scattered light at a known frame rate that were then animated in sequence to create videos. An open-source code (PIVlab) tracked individual particles from image to image and stitched an overlay onto the images, creating a visualization of fluid flow and allowing us to determine the speed of the particles. Assuming that the particles moved at the same velocity as the fluid around them, we created a spatial representation of the velocity field surrounding the robot.

3.3 Robot Setup

The robot presented in this thesis is tethered to a platform outside of the water, eliminating the need for the system electronics to either be submersible or contained in a waterproof housing. The pump and valve manifold, in line with each other, were located on a plate above the water channel and polyurethane tubing carried the water from the valves on the platform to both the morphing body and the four legs. A secondary water tank outside of the water channel supplied water to the inlet of the hydraulic pump. The discharge lines used to vent water pressure in the legs (bringing the legs back to the neutral position) and the pressure relief line of the valve manifold also fed into this secondary tank. This effectively made the robot, pump, valves, and secondary tank a closed system, which prevented any debris in the system from contaminating the water in the water channel. The closed system also keeps flow into the pump and out from the exhaust lines from creating any turbulence or altering the flow patterns in the channel that would affect either the robot or the measurement instrumentation. A diagram of this setup is provided in Fig. 3.2.

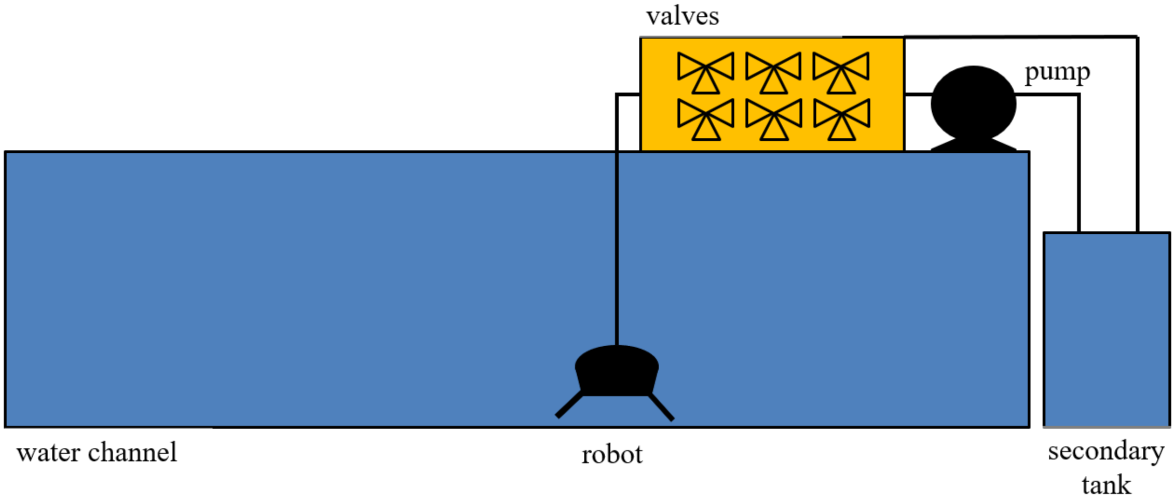

Figure 3.2: Diagram of the robot and supporting fluid systems. Since the electronic flow control hardware (valves and hydraulic pump) are not submersible, a tether ran from the robot in the water channel to the other hardware in air.

Chapter 4

Static Characterization

4.1 Computational Fluid Dynamics Simulation

I modeled several simple shapes based on the shapes tested in the water tunnel to predict the lift and drag forces experienced by the robot. I used computational fluid dynamics (CFD) software (Fluent, ANSYS) to simulate the flow over 2D cross-sections of representative shapes. The software modeled the flow velocity distribution and pressure distribution over the robot body and calculated the hydrodynamic lift and drag forces (Fig. 4.1). I only simulated flow around the body as including the legs in a 2D simulation would have prevented any consideration of the flow underneath the body. The CFD simulation used the same parameters as the experiments performed in the water channel, such as flow speed $0.12\,\mathrm{m/s}$. The k-kl-omega model is appropriate for low Reynolds numbers in the transition region between laminar and turbulent flow, as is present at the bottom of the water channel.

I systematically varied the dimensions of the robot body to examine the relationship between body shape and lift and drag forces on the robot. The cases in which the morphed body is on the side opposite incoming flow are separate from the cases in which the morphed body is on the side of incoming flow as this significantly changes the flow over the body (Figs. 4.2 and

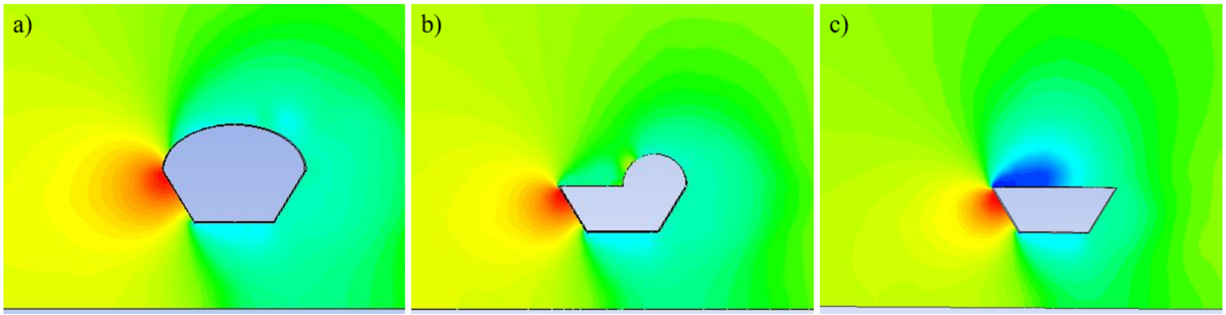

Figure 4.1: CFD simulation of the pressure distribution over the three robot bodies. The simulations of the pressure distribution over a) the symmetric body, b) the asymmetric body, and c) the flat body estimate the hydrodynamic forces on each body shape.

4.3).

When the morphed body is on the side opposite incoming flow, varying the height of the morphing body changes the drag force experienced while varying the length of the morphing body causes differences in the lift force experienced. If the morphing body is tall, the drag coefficient is higher than if the morphing body is short; the flat body being an exception with its sharp corners. If the morphing body is long in length, the coefficient of lift is positive and the lift force on the robot is upward; however, if the morphing body is short in length, the coefficient of lift is negative and the lift force is downward. The ability to change lift direction is desirable because downward lift increases the friction between the robot and the ground and is advantageous for station-keeping while upward lift decreases friction and is advantageous for moving with the flow.

When the morphed body is on the side closest to incoming flow, varying the height of the morphing body changes both the lift and drag forces experienced by the robot while varying the length of the body primarily changes the drag forces experienced. If the morphing body is tall, the lift coefficient is lower and the drag coefficient is higher than if the morphing body is short. If the morphing body is long in length, the drag coefficient is higher than if the morphing body is short. The range of lift coefficients possible with the morphing body facing flow is close to half of the corresponding range with the morphing body opposite flow, while the range of drag coefficients is similar in both cases.

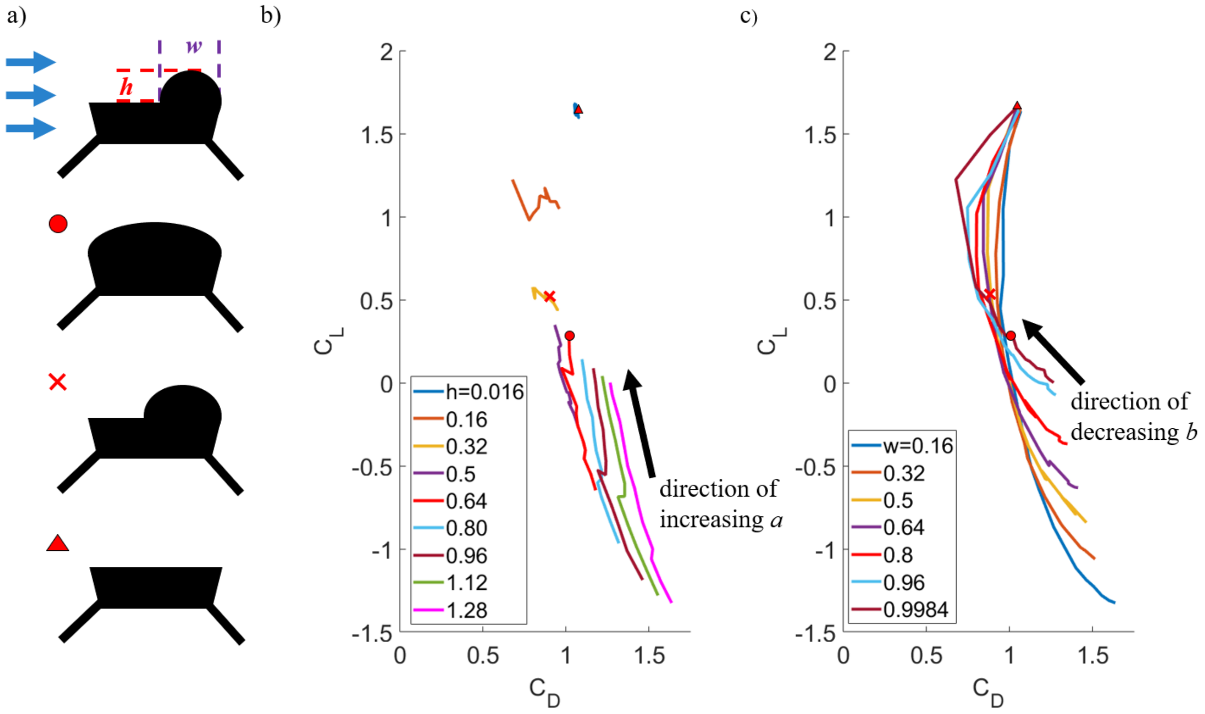

Figure 4.2: Comparison of coefficient of lift and coefficient of drag for varied geometry (lengths normalized to overall body length) of the morphing body. Points are overlaid to denote the where the simulation uses the geometries of the morphing body that were tested in the water channel. a) shows a diagram of the robot with the dimensions that can be changed and the geometries tested physically, b) plots coefficient of drag against coefficient of lift where each trace is a constant body height with varied body lengths, and c) plots coefficient of drag against coefficient of lift where each trace is a constant body length with varied body heights.

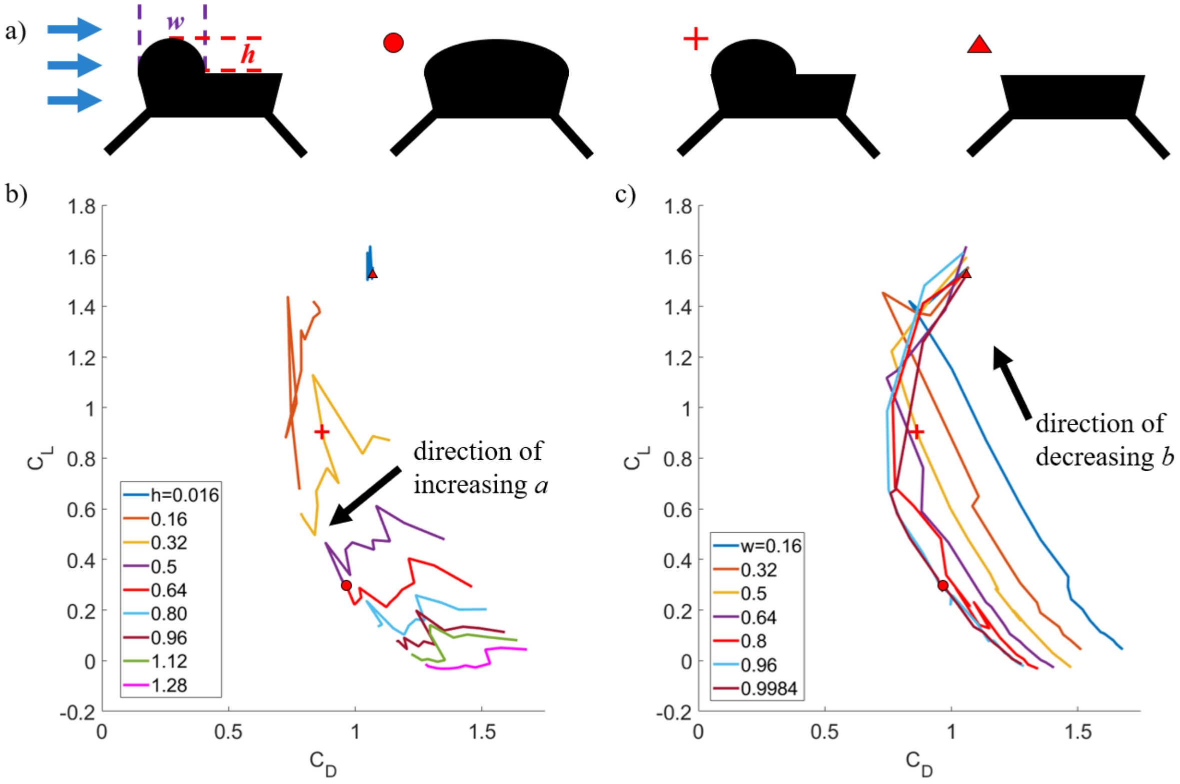

Figure 4.3: Comparison of coefficient of lift and coefficient of drag for varied geometry (lengths normalized to overall body length) of the morphing body. Points are overlaid to denote the where the simulation uses the geometries of the morphing body that were tested in the water channel. a) shows a diagram of the robot with the dimensions that can be changed and the geometries tested physically, b) plots coefficient of drag against coefficient of lift where each trace is a constant body height with varied body lengths, and c) plots coefficient of drag against coefficient of lift where each trace is a constant body length with varied body heights.

4.2 Experimental Flow Visualization

I used the particle image velocimetry data to experimentally characterize the flow over the tops of the different morphed structures. We took sequences of 150 images with a high-resolution camera at rates ranging from five to thirty frames per second and then used commercial software (Mathworks, MATLAB) to stitch the images together into video and to highlight the streamlines. Since the robot is approximately the size of the laser field used, the field was not large enough to image both the flow over the whole morphing structure and flow over the trailing edge, necessitating multiple measurements (Fig. 4.4).

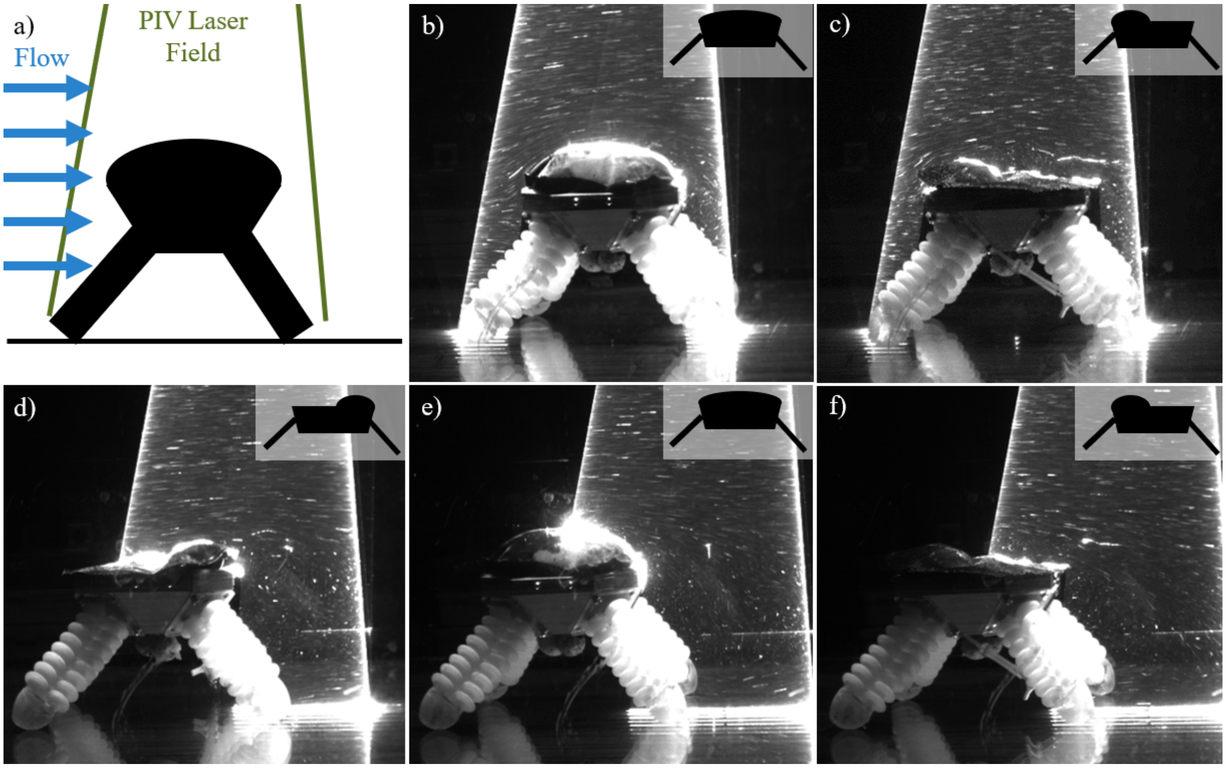

Figure 4.4: Particle image velocimetry data with the flow moving from left to right over the robot with different morphing structures. a) A schematic of a representative PIV measurement setup. b) and e) PIV visualization of flow over and past the large-morphed structure. c) and f): PIV visualization of flow over and past the semi-morphed structure on the leading edge of the robot. d) PIV visualization of flow vortices behind the trailing edge of the semi-morphed structure.

The PIV imaging shows that the flow closely follows the morphed surface over the body. Because the soft pouch actuator forms a continuous contour without sharp corners or discontinuities, the flow over the morphed structure is smooth and does not separate. Flow separation causes turbulence from that location onward, which contributes to the drag force on the body. The flow separates at the trailing edge of each of the morphed structures, indicating significant turbulence only occurs behind that structure. For the flat structure, the large-morphed structure, and the semi-morphed structure with the morph on the trailing edge, this results in flow separation and turbulence generation behind the robot as a whole. However, with the semi-morphed structure on the leading edge, the flow separation and turbulence generation occurs over the top of the robot, which can lead to increased drag. In addition, this PIV data reasonably matches the streamlines created by the CFD simulation (Fig. 4.5). Because the PIV image is a sideview image of a 3D system, the image also captures some of the flow passing over the surface as it tapers off out of the plane. The CFD simulation case is simplified by the 2D assumption and does not capture flow out of the plane so the flow representation generated by the simulation shows flow separation that is similar to, but not exactly the same as was recorded experimentally.

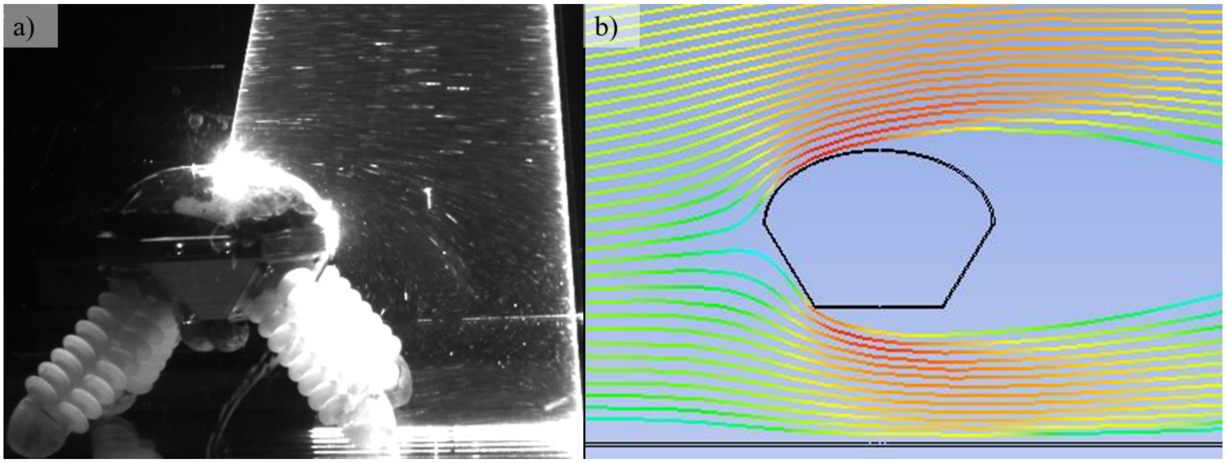

Figure 4.5: Comparison of flow streamlines a) captured experimentally using PIV and b) generated by the CFD simulation.

4.3 Effect of Morphing on Resistance to Sliding in Flow

We subjected the three morphed configurations to steadily increasing flow to determine the flow speed at which the stationary (non-walking) robot would begin to slide in the direction of flow. Since the rigid frame, leg and foot design, and leg angle were constant during all the tests, the changes in the morphing structure interacting with flow caused the differences in the critical velocity for sliding. To test the orientation dependence of each structure, we rotated each body and morphing structure by 180° to examine the differences between going with flow and against flow (Fig. 4.6).

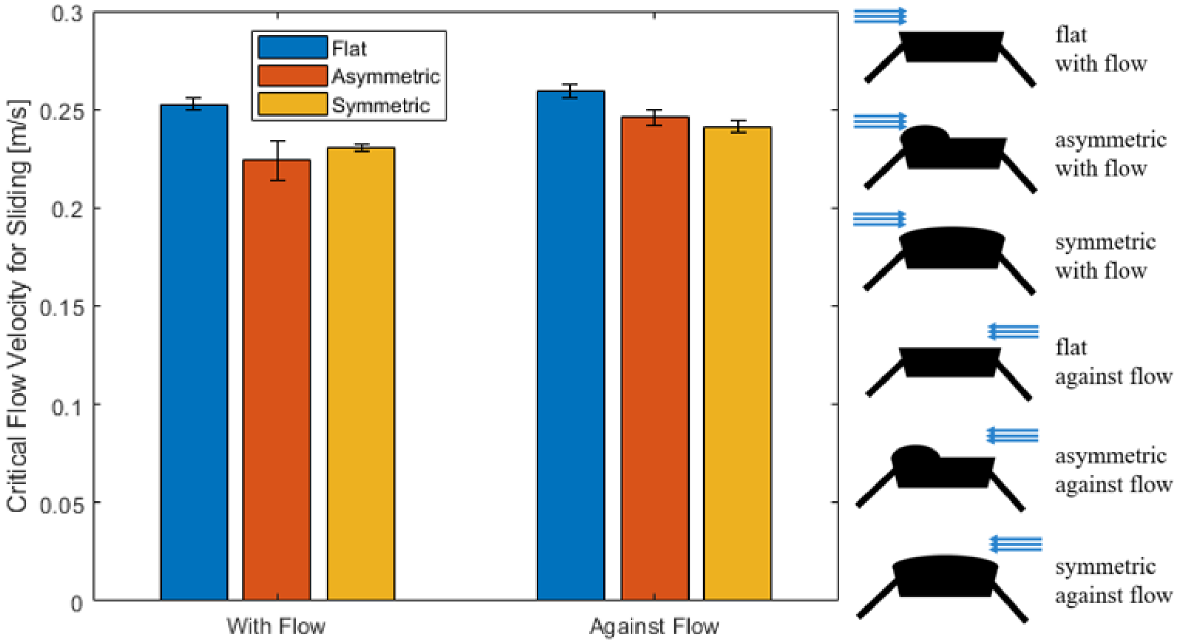

Figure 4.6: Data comparing the critical flow speed necessary to cause the stationary robot with different bodies to start sliding. This critical flow speed was similar with and against flow for symmetric body shapes, but not for asymmetric body shapes. Smaller body shapes caused the robot to be more resistant to sliding.

The flat structure required the highest flow rate to induce sliding. Since the morphed structure was uninflated, it has a shorter overall height than the other structures, decreasing the cross-sectional area of the surface in contact with flow and reducing the drag on the body. These results are consistent in both directions, indicating that the flat structure has no orientation bias. The symmetrically morphed structure requires a significantly lower flow speed to induce sliding, indicating that the drag on this body is much higher than the drag on the flat structure. There was a small amount orientation bias in the large-morphed structure, even though it was intended to be symmetric.

Unlike the other two structures, the semi-morphed structure had a clear orientation bias. When the inflated half is on the leading edge of the robot, a lower flow speed is required to cause sliding, but when the inflated half is on the trailing edge of the robot, sliding occurs at a higher flow rate. Two other factors influence this discrepancy. First, when the morphed structure is on the leading edge of the robot, there is flow separation over the body instead of behind the body, increasing turbulence and drag over the surface. Second, when the morphed structure is on the trailing edge of the robot, it likely generates some downward lift, much like a cambered airfoil would create.

The orientation bias for the semi-morphed structure also creates a difference between that shape and the fully-inflated shape. When the semi-morphed structure is on the leading edge of the robot, it is less resistant to sliding than the fully inflated structure and when the semi-morphed structure is on the trailing edge of the robot it is more resistant to sliding than the fully-inflated structure. This phenomenon is useful in a practical system because when walking with flow more sliding would be beneficial to aid in locomotion, and when walking against flow, less sliding would be desired to prevent being pushed backward. A two-factor analysis of variance (ANOVA) test showed that both the flow direction and the morphing structure shape affect the critical flow velocity for sliding and that the flow direction influences how much each morphing shape affects the critical flow velocity for sliding (Table 4.1). This trend indicates that the ability to morph the robot into different shapes has advantages with respect to simple morphing between two shapes.

I attribute some of the variance in results to imperfect manufacturing of the pouches causing unintended asymmetry, which can be seen when visually inspecting the pouches. This

Table 4.1: Two-Way Analysis of Variance (ANOVA) for Critical Sliding Velocity

Source	SS	df	MS	F	Prob > F
Morphing Structure Shape	0.00171	2	0.00086	32.89	0
Flow Direction	0.00079	1	0.00079	30.34	0.0001
Interaction	0.00019	2	0.00009	3.55	0.0615
Error	0.00031	12	0.00003		
Total	0.003	17			

asymmetry can lead to an unintended orientation dependence or can contribute to rotation of the robot instead of translation. Other sources of variance include stochasticity of the flow speeds during flow acceleration and inconsistent step size of the flow acceleration. The flow velocity was set using a potentiometer dial with markers, so consistent size acceleration steps were difficult to obtain.

To compare the CFD simulations with the experimental critical velocity, I created a force balance to determine the forces needed to cause sliding. Based on the free body diagram shown in Fig. 4.7, the robot will start sliding when the friction force between the feet and the ground can no longer balance the drag force on the body. This point can be found using a force balance in the horizontal direction:

$$\Sigma F_X = F_D + \mu N = 0 \tag{4.1}$$

where F_D is the drag force (calculated by the CFD simulation), μ is the friction coefficient (measured experimentally), and N is the normal force on the robot. The normal force is determined using the sum of the forces in the vertical direction:

$$\Sigma F_X = F_B + F_L - F_G + N = 0 \tag{4.2}$$

where F_B is the buoyant force (calculated from volume of fluid displaced), F_L is the lift force (calculated by the CFD simulation), and F_G is the gravitational force (measured experimentally).

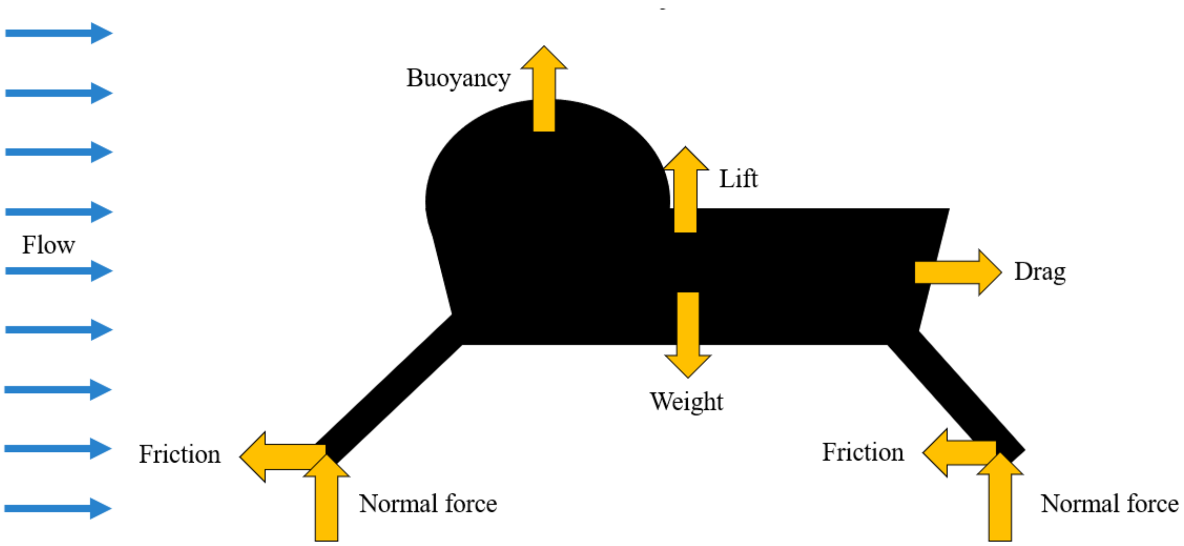

Figure 4.7: Free body diagram of the stationary robot. Because this analysis only considers the force balances on the robot, the location of the forces on the robot are not considered.

Rearranging this expression for N and substituting into Eq. 4.1:

$$F_D = \mu(F_G - F_B - F_L) \tag{4.3}$$

and the robot begins to slide when the combination of drag and lift forces satisfy the following inequality:

$$F_D + \mu F_L > \mu(F_G - F_B) \tag{4.4}$$

To determine the flow speed at which Eq. 4.4 holds true, I performed CFD simulations at different flow velocities for the robot shapes tested in the water channel. These are compared to the experimentally-determined critical flow velocities in Fig. 4.8.

The simulation values are consistently lower than the experimental results, indicating that the simulated robot is less resistant to sliding in flow than the physical robot. I attribute the discrepancies between the experimental critical flow velocity and the simulated critical velocity to the simplifications made when constructing the CFD simulations. The 2D assumption assumes the robot has a constant height along the depth into the plane, creating a shape more similar to

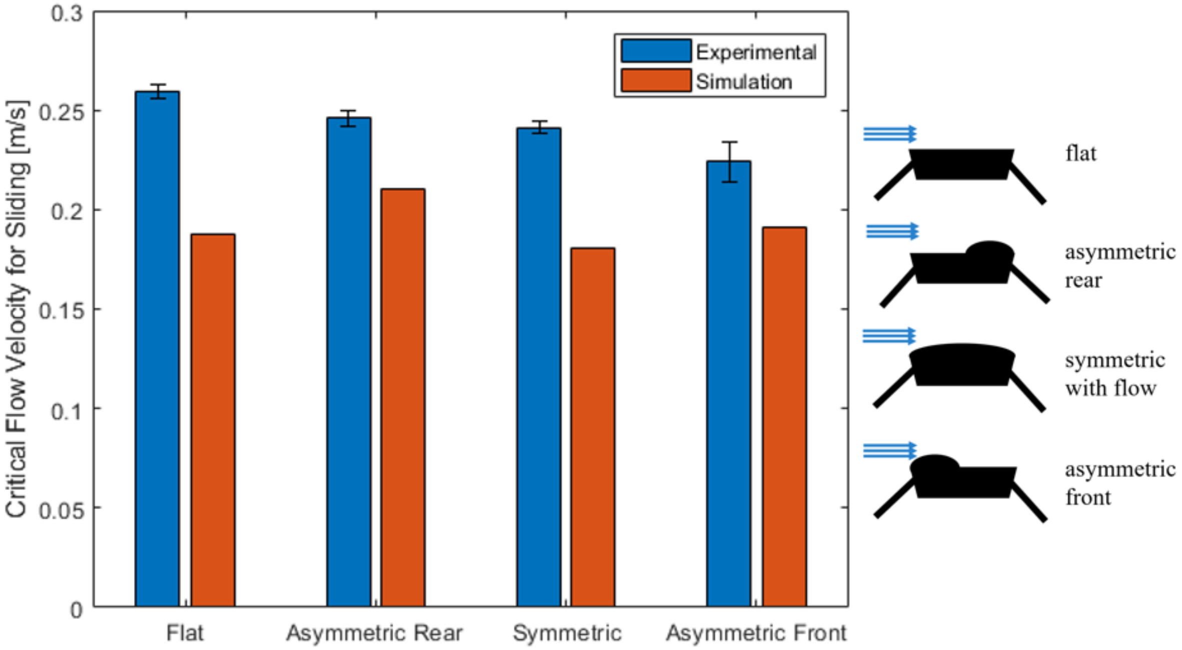

Figure 4.8: Comparison of simulation data and experimental data for critical flow speed necessary to cause the stationary robot to start sliding for different bodies.

a cylinder than the actual dome shape. In addition, the effects of the legs on flow underneath the robot as well are not considered with this 2D simulation as including legs would completely prevent the flow from traveling under the robot. Flow under the robot is important in determining the amount of lift on the system, and unmodeled turbulence under the robot might be a large source of error.

Chapter 5

Morphing Structure During Dynamic Operation

5.1 Effect of Morphing Structure on Walking

We measured the walking speed of the robot with different morphing structure configurations when in still water and when walking in the same direction of flow below the point at which sliding begins. Since the body sways during walking, the angle of attack of the morphing structure can change periodically, which affects the drag and downforce on the robot.

In still water, the different bodies created no difference in robot speed walking with flow. With no flow, the robot walked around $15\,\mathrm{mm/s}$ which was likely not fast enough for the body shape to significantly affect the fluid forces. However, when walking in the direction of flow, the morphing structure had a noticeable effect on the walking speed of the robot (Fig. 5.1) as the speed of the fluid flow is an order of magnitude faster than the speed of the walking robot. The robot walked the most slowly with the flat structure, the fastest with the large-morphed structure, and had an intermediate speed with the semi-morphed structure. As with the sliding experiment, the flow pushed the large-morphed structure more than the others and pushed the flat structure the least. This caused the robot to walk fastest with the large-morphed structure and slowest with the flat structure. The robot walking speed with semi-morphed structure was in between these extremes.

Variances in this experiment were likely due to the effect of the flow on the hydraulic tether. The tether caused additional drag on the robot, which was less consistent than the actual drag on the morphing structure. This caused variance in the magnitude of the robot speed, but did not affect the trend. The robot was not able to walk against flow with any of the morphing structures because the minimum flow speed of the water channel was higher than that which the robot could walk against. I would expect the robot to be able to walk into flow of less than half the flow speed observed to cause sliding since half of the feet are in contact and generate friction during walking but since this speed was less than the water channel minimum, we were unable to test at that flow speed.

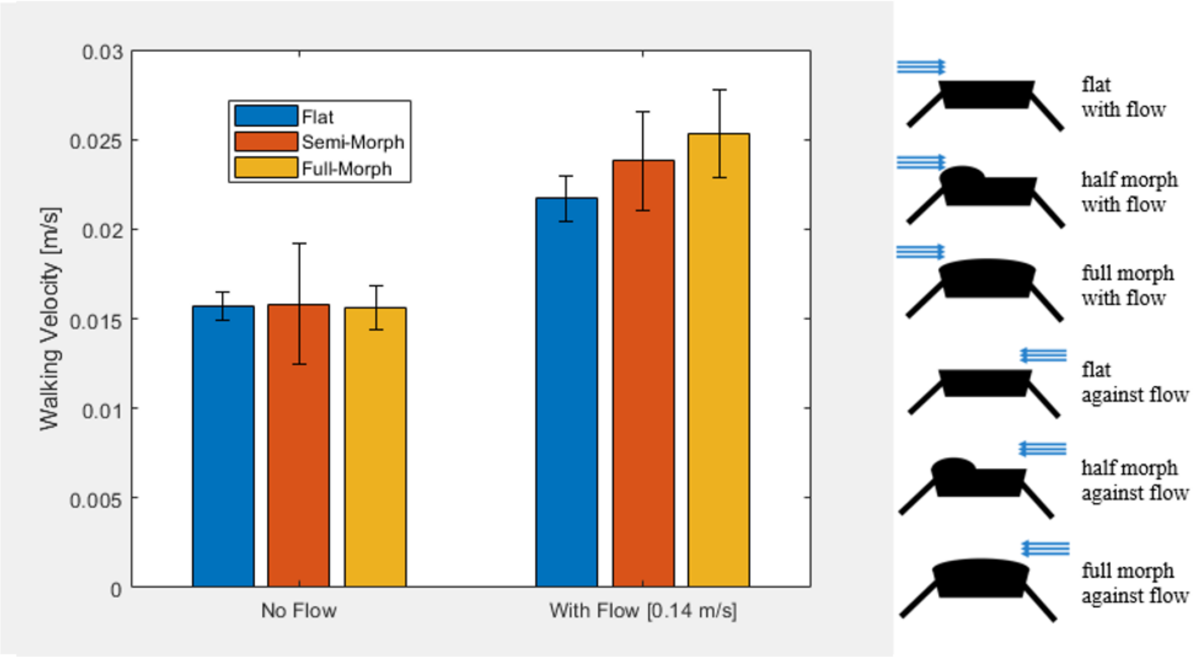

Figure 5.1: Data comparing speed of the robot with different bodies in still water and with flow. In no flow, body shape had little effect on robot speed while when walking with flow, robots with larger bodies walked faster.

5.2 Morphing in Response to Flow Change

An active morphing structure is able to adjust its shape during robot operation when advantageous as a response to sensed changes in the environment. Using a commercial force sensor, (5.2) the robot can sense flow above or below predetermined thresholds and can then morph its body into a more desirable configuration. We demonstrated this response with a simple experiment: when high flow is sensed, the robot morphs its body from the large-morphed state that is likely to slide to the flat state that is less likely to slide (Fig. 5.3).

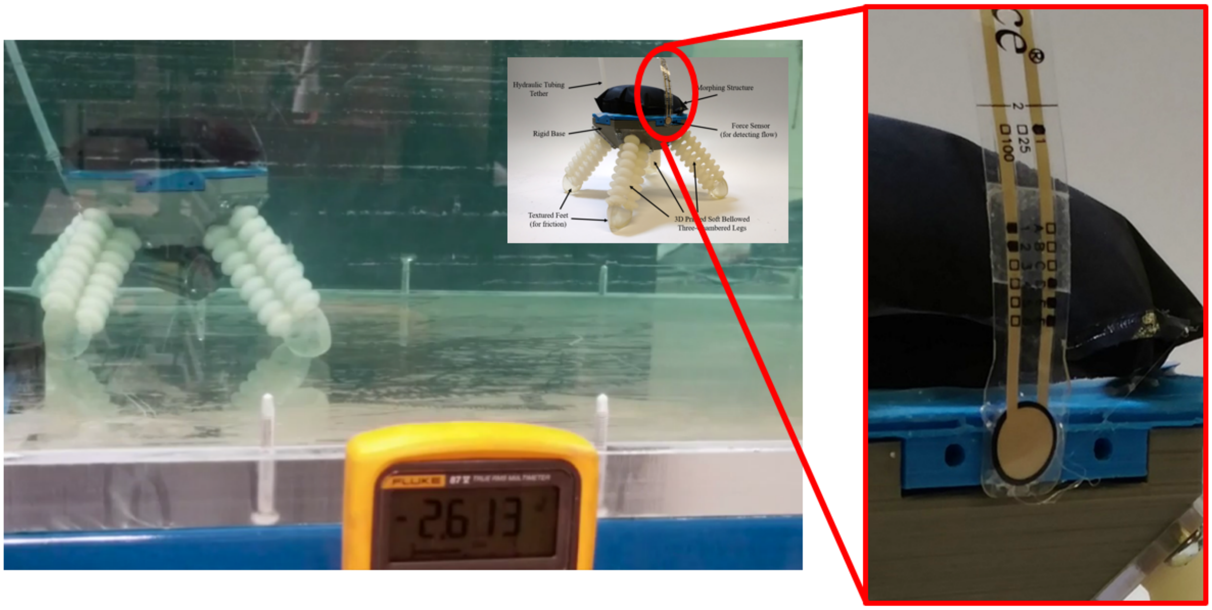

Figure 5.2: The commercial commercial force sensor attached to the front of the robot.

We placed the robot in the water channel with the force sensor facing the direction of flow. The morphed structure was in the fully inflated state and the channel was on a low flow setting, which resulted in a sensor reading of approximately 2.6 V. We then manually increased the flow speed above the speed at which we previously determined that the robot would slide, which resulted in a sensor reading of approximately 2.9 V. This was a significant change in sensor reading used as a threshold at which the valve vented water from the morphing structure, deflating it to the fully flat shape.

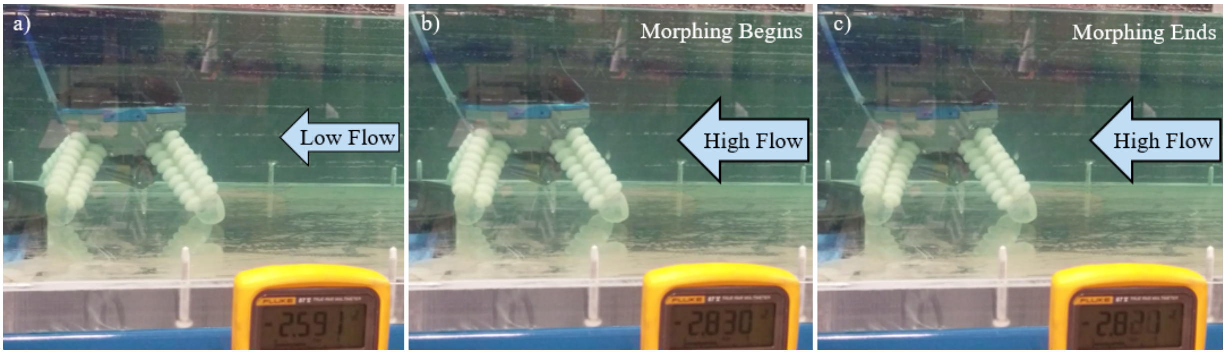

Figure 5.3: The robot with force sensor detecting increased flow and morphing its body to compensate. a) Robot with large-morphed structure and sensor reading in low flow. b) Robot with large-morphed structure after flow increased - note increased sensor reading and taller leg posture in higher flow. c) Robot after the large-morphed structure was deflated to the flat structure in the same higher flow.

This demonstrates that a morphable robot with sensing capability can mitigate the effects of disadvantageous flow by adjusting its shape. A calibration between the flow speed and the force sensed is needed to more accurately understand how sensitive the sensor is to flow changes, although we have not yet done this for cases outside this demonstration.

5.3 Morphing for Control of Robot Locomotion

We also demonstrated the use of the morphing structure to control the robot's locomotion by showing it can morph its body to help stop locomotion. In previous experiments, we showed that the robot with the fully inflated body shape would walk fastest in the same direction as flow, but would conversely be least resistant to sliding when not walking. In this experiment, we created a scenario where the robot with the large shape was walking with flow, but wanted to stop at a certain place in space.

Since the robot was walking with flow, the body was fully inflated so that it would walk the fastest. When the robot stopped walking to try to land on the target line without changing its body shape, the flow continued to slide the robot along the bottom of the channel and it was unable to stop at all. However, when the robot deflated its morphing structure to the flat shape as it stopped walking, the change in shape allowed it to come to a stop on the target line instead of sliding past. This active adjustment of robot body shape demonstrates that the morphing structure can be used to directly control robot locomotion and allows for finer control of robot behavior as it can be less susceptible to strong fluid forces underwater.

Chapter 6

Conclusions

In this thesis I have presented a robot with soft legs and a morphing body that can change its shape when a change in flow is encountered. I have shown that a morphing structure that can actively respond to flow conditions will create favorable hydrodynamic characteristics. A robot body with a large profile shape will move faster when walking in the same direction as flow while a robot with a lower profile shape will be more resistant to sliding when attempting to maintain a stationary position within the flow. Thus, a morphing structure that can sense flow and switch between states would be more efficient when encountering fluid forces. This concept is applicable to many other underwater systems that wish to adapt to changing flow characteristics and leverages the advantages of soft actuators to form a continuous surface for interaction with flow. In the future, a robot with a more complex morphing body can actively sense the changes in flow speed and direction around it and can morph its shape to continuously present the most hydrodynamically effective profile toward the flow.

Next steps for development of this robot would be to focus on adapting the current system for more practical uses. A full characterization of the flow sensor would provide more precise control over robot locomotion. Using negative pressure instead of positive pressure could increases the lifetimes of the actuators, making it more suitable for active deployment. Developing a fully

3D printed body and incorporating 3D printed soft sensing could leverage the full capabilities of additive manufacturing for creating complex geometries in a single manufacturing step. In addition, having the morphing structure on the top of the robot can create a waterproof enclosure in which electronics and power components could be stored to make the system fully untethered.

Creating an untethered system is also one of the next steps for improving the experimental characterization of the robot as it eliminates some of the variance in measurement from the hydraulic and electronic tether. In addition, expanding the CFD simulations will provide additional information about the way the morphing body interacts with flow and future work would include extending the simulation from 2D to 3D. Other next steps would include determining the coefficients of lift and drag of the various bodies independent of the legs and separating the effects of lift, downforce, and drag on the robot locomotion. This will allow us to perform additional modeling of fluid interactions with the body and to connect the experimental results with the model. Other researchers can use these results to inform design decisions for future improved morphing structures.

Active shaping of an underwater walking robot can generalize to many different systems. Other underwater crafts like ROVs and unmanned underwater vehicles (UUVs) could also benefit from adaptable hydrodynamic characteristics. With active control of lift and drag on the body, robots can be more successful both moving and holding a constant position. Morphing structures have the potential to increase the efficiency of any stem that moves through fluid.

This thesis, in part, is currently being prepared for submission for publication of the material. Ishida, Michael; Drotman, Dylan; Shih, Benjamin; Hermes, Mark; Luhar, Mitul; Tolley, Michael T. The thesis author was the primary investigator and author of this material.

Bibliography

[1] A. Thomas, M. Milano, M. G. G'Sell, K. Fischer, and J. Burdick, "Synthetic jet propulsion for small underwater vehicles," in *Robotics and Automation, 2005. ICRA 2005. Proceedings of the 2005 IEEE International Conference on*, pp. 181–187, IEEE, 2005.

[2] F. Azis, M. Aras, M. Rashid, M. Othman, and S. Abdullah, "Problem identification for underwater remotely operated vehicle (rov): A case study," *Procedia Engineering*, vol. 41, pp. 554–560, 2012.

[3] J. Siekmann, "On a pulsating jet from the end of a tube, with application to the propulsion of certain aquatic animals," *Journal of Fluid Mechanics*, vol. 15, no. 3, pp. 399–418, 1963.

[4] M. Sfakiotakis, D. M. Lane, and J. B. C. Davies, "Review of fish swimming modes for aquatic locomotion," *IEEE Journal of oceanic engineering*, vol. 24, no. 2, pp. 237–252, 1999.

[5] J. Ayers, "Underwater walking," *Arthropod structure & development*, vol. 33, no. 3, pp. 347–360, 2004.

[6] G. Kerkut, "The forces exerted by the tube feet of the starfish during locomotion," *Journal of Experimental Biology*, vol. 30, no. 4, pp. 575–583, 1953.

[7] M. M. Martinez, R. Full, and M. Koehl, "Underwater punting by an intertidal crab: a novel gait revealed by the kinematics of pedestrian locomotion in air versus water," *Journal of Experimental Biology*, vol. 201, no. 18, pp. 2609–2623, 1998.

[8] M. A. Ashley-Ross, R. Lundin, and K. L. Johnson, "Kinematics of level terrestrial and underwater walking in the california newt, taricha torosa," *Journal of Experimental Zoology Part A: Ecological and Integrative Physiology*, vol. 311, no. 4, pp. 240–257, 2009.

[9] K. Karakasiliotis, R. Thandiackal, K. Melo, T. Horvat, N. Mahabadi, S. Tsitkov, J. Cabelguen, and A. Ijspeert, "From cineradiography to biorobots: an approach for designing robots to emulate and study animal locomotion," *Journal of The Royal Society Interface*, vol. 13, no. 119, p. 20151089, 2016.

[10] A. Vidal-Gadea, M. Rinehart, and J. Belanger, “Skeletal adaptations for forwards and sideways walking in three species of decapod crustaceans,” *Arthropod structure & development*, vol. 37, no. 2, pp. 95–108, 2008.

[11] M. Weissburg, C. James, D. Smee, and D. Webster, “Fluid mechanics produces conflicting, constraints during olfactory navigation of blue crabs, callinectes sapidus,” *Journal of Experimental Biology*, vol. 206, no. 1, pp. 171–180, 2003.

[12] K. J. Hayne and A. R. Palmer, “Intertidal sea stars (pisaster ochraceus) alter body shape in response to wave action,” *Journal of Experimental Biology*, vol. 216, no. 9, pp. 1717–1725, 2013.

[13] S. Steele, J. Dahl, G. Weymouth, and M. Triantafyllou, “Shape of retracting foils that model morphing bodies controls shed energy and wake structure,” *Journal of Fluid Mechanics*, vol. 805, pp. 355–383, 2016.

[14] E. G. Drucker and G. V. Lauder, “A hydrodynamic analysis of fish swimming speed: wake structure and locomotor force in slow and fast labriform swimmers,” *Journal of Experimental Biology*, vol. 203, no. 16, pp. 2379–2393, 2000.

[15] A. Packard, “Jet propulsion and the giant fibre response of loligo,” *Nature*, vol. 221, no. 5183, p. 875, 1969.

[16] A. Arienti, M. Calisti, F. Giorgio-Serchi, and C. Laschi, “Poseidrone: design of a soft-bodied rov with crawling, swimming and manipulation ability,” in *Oceans-San Diego, 2013*, pp. 1–7, IEEE, 2013.

[17] F. Corucci, M. Calisti, H. Hauser, and C. Laschi, “Novelty-based evolutionary design of morphing underwater robots,” in *Proceedings of the 2015 annual conference on Genetic and Evolutionary Computation*, pp. 145–152, ACM, 2015.

[18] J. Pikul, S. Li, H. Bai, R. Hanlon, I. Cohen, and R. Shepherd, “Stretchable surfaces with programmable 3d texture morphing for synthetic camouflaging skins,” *Science*, vol. 358, no. 6360, pp. 210–214, 2017.

[19] E. Steltz, A. Mozeika, N. Rodenberg, E. Brown, and H. M. Jaeger, “Jsel: Jamming skin enabled locomotion,” in *Intelligent Robots and Systems, 2009. IROS 2009. IEEE/RSJ International Conference on*, pp. 5672–5677, IEEE, 2009.

[20] H.-J. Kim, S.-H. Song, and S.-H. Ahn, “A turtle-like swimming robot using a smart soft composite (ssc) structure,” *Smart Materials and Structures*, vol. 22, no. 1, p. 014007, 2012.

[21] J. Colorado, A. Barrientos, C. Rossi, and K. S. Breuer, “Biomechanics of smart wings in a bat robot: morphing wings using sma actuators,” *Bioinspiration & biomimetics*, vol. 7, no. 3, p. 036006, 2012.

[22] P. Jagadeesh, K. Murali, and V. Idichandy, "Experimental investigation of hydrodynamic force coefficients over auv hull form," *Ocean engineering*, vol. 36, no. 1, pp. 113–118, 2009.

[23] G. Krummel, K. N. Kaipa, and S. K. Gupta, "A horseshoe crab inspired surf zone robot with righting capabilities," in *ASME 2014 International Design Engineering Technical Conferences and Computers and Information in Engineering Conference*, pp. V05AT08A010–V05AT08A010, American Society of Mechanical Engineers, 2014.

[24] B.-H. Jun, H. Shim, J.-Y. Park, B. Kim, and P.-M. Lee, "A new concept and technologies of multi-legged underwater robot for high tidal current environment," in *Underwater Technology (UT), 2011 IEEE Symposium on and 2011 Workshop on Scientific Use of Submarine Cables and Related Technologies (SSC)*, pp. 1–5, IEEE, 2011.

[25] C. Georgiades, M. Nahon, and M. Buehler, "Simulation of an underwater hexapod robot," *Ocean Engineering*, vol. 36, no. 1, pp. 39–47, 2009.

[26] S. N. Singh, A. Simha, and R. Mittal, "Biorobotic auv maneuvering by pectoral fins: inverse control design based on cfd parameterization," *IEEE Journal of Oceanic Engineering*, vol. 29, no. 3, pp. 777–785, 2004.

[27] M. Sfakiotakis, A. Kazakidi, N. Pateromichelakis, J. A. Ekaterinaris, and D. P. Tsakiris, "Robotic underwater propulsion inspired by the octopus multi-arm swimming," in *Robotics and Automation (ICRA), 2012 IEEE International Conference on*, pp. 3833–3839, IEEE, 2012.

[28] D. Rus and M. T. Tolley, "Design, fabrication and control of soft robots," *Nature*, vol. 521, no. 7553, p. 467, 2015.

[29] A. D. Marchese, R. K. Katzschmann, and D. Rus, "A recipe for soft fluidic elastomer robots," *Soft Robotics*, vol. 2, no. 1, pp. 7–25, 2015.

[30] F. Connolly, C. J. Walsh, and K. Bertoldi, "Automatic design of fiber-reinforced soft actuators for trajectory matching," *Proceedings of the National Academy of Sciences*, vol. 114, no. 1, pp. 51–56, 2017.

[31] B. Mosadegh, P. Polygerinos, C. Keplinger, S. Wennstedt, R. F. Shepherd, U. Gupta, J. Shim, K. Bertoldi, C. J. Walsh, and G. M. Whitesides, "Pneumatic networks for soft robotics that actuate rapidly," *Advanced functional materials*, vol. 24, no. 15, pp. 2163–2170, 2014.

[32] C.-P. Chou and B. Hannaford, "Measurement and modeling of mckibben pneumatic artificial muscles," *IEEE Transactions on robotics and automation*, vol. 12, no. 1, pp. 90–102, 1996.

[33] R. V. Martinez, J. L. Branch, C. R. Fish, L. Jin, R. F. Shepherd, R. Nunes, Z. Suo, and G. M. Whitesides, "Robotic tentacles with three-dimensional mobility based on flexible elastomers," *Advanced materials*, vol. 25, no. 2, pp. 205–212, 2013.

[34] P. Glick, S. Suresh, D. Ruffatto III, M. Cutkosky, M. T. Tolley, and A. Parness, “A soft robotic gripper with gecko-inspired adhesive,” *IEEE Robotics and Automation Letters*, 2018.

[35] M. Calisti, F. Corucci, A. Arienti, and C. Laschi, “Dynamics of underwater legged locomotion: modeling and experiments on an octopus-inspired robot,” *Bioinspiration & biomimetics*, vol. 10, no. 4, p. 046012, 2015.

[36] M. Cutkosky, J. Jourdain, and P. Wright, “Skin materials for robotic fingers,” in *Robotics and Automation. Proceedings. 1987 IEEE International Conference on*, vol. 4, pp. 1649–1654, IEEE, 1987.

[37] J. Akizono, T. Tanaka, K. Nakagawa, T. Tsuji, and M. Iwasaki, “Seabottom roughness measurement by aquatic walking robot,” in *OCEANS’97. MTS/IEEE Conference Proceedings*, vol. 2, pp. 1395–1398, IEEE, 1997.

[38] H. Greiner, A. Shectman, C. Won, R. Elsley, and P. Beith, “Autonomous legged underwater vehicles for near land warfare,” in *Autonomous Underwater Vehicle Technology, 1996. AUV’96., Proceedings of the 1996 Symposium on*, pp. 41–48, IEEE, 1996.

[39] J.-Y. Kim and B.-H. Jun, “Design of six-legged walking robot, little crabster for underwater walking and operation,” *Advanced Robotics*, vol. 28, no. 2, pp. 77–89, 2014.

[40] M. Calisti, E. Falotico, and C. Laschi, “Hopping on uneven terrains with an underwater one-legged robot,” *IEEE Robotics and Automation Letters*, vol. 1, no. 1, pp. 461–468, 2016.

[41] G. Wang, X. Chen, S. Yang, P. Jia, X. Yan, and J. Xie, “Subsea crab bounding gait of leg-paddle hybrid driven shoal crablike robot,” *Mechatronics*, vol. 48, pp. 1–11, 2017.

[42] D. Drotman, S. Jadhav, M. Karimi, and M. T. Tolley, “3d printed soft actuators for a legged robot capable of navigating unstructured terrain,” in *Robotics and Automation (ICRA), 2017 IEEE International Conference on*, pp. 5532–5538, IEEE, 2017.